

Geophysical Research Letters

RESEARCH LETTER

10.1029/2019GL082041

Key Points:

- The 2018 earthquake ruptured within the underthrust Pacific slab at depths from 45 to 60 km just north of Anchorage
- The preferred fault dips 65 degrees westward and the strike is 186 degrees, with the rupture expanding northward, away from Anchorage
- The source is located near the intraslab lateral transition from underthrust thick Yakutat terrane to normal Pacific plate

Supporting Information:

- · Supporting Information S1
- · Data Set S1
- · Data Set S2

Correspondence to:

T. Lay, tlay@ucsc.edu

Citation:

Liu, C., Lay, T., Xie, Z., & Xiong, X. (2019). Intraslab deformation in the 30 November 2018 Anchorage, Alaska, M_W 7.1 earthquake. *Geophysical Research Letters*, 46, 2449–2457. https://doi.org/10.1029/2019GL082041

Received 13 JAN 2019 Accepted 20 FEB 2019 Accepted article online 25 FEB 2019 Published online 4 MAR 2019

Intraslab Deformation in the 30 November 2018 Anchorage, Alaska, M_W 7.1 Earthquake

Chengli Liu^{1,2} D, Thorne Lay² D, Zujun Xie¹, and Xiong Xiong¹ D

¹Hubei Subsurface Multi-Scale Imaging Key Laboratory, Institute of Geophysics and Geomatics, China University of Geosciences, Wuhan, China, ²Department of Earth and Planetary Sciences, University of California, Santa Cruz, CA, USA

Abstract Anchorage, Alaska, was strongly shaken on 30 November 2018 by an M_W 7.1 earthquake that ruptured within the underthrust Pacific plate at depths of from 45 to 65 km. Ground failures occurred in saturated lowlands filled with sediments, producing notable road damage, but there was limited structural damage in Anchorage, only ~12 km south of the epicenter. The earthquake has a normal faulting geometry with a shallowly dipping east-west tension axis indicating intraslab deformation, likely between the underthrust Yakutat terrane and adjacent Pacific seafloor. Separate and joint inversions of teleseismic P and SH waves, regional strong ground motions, and GPS static displacements provide a weak preference for a westward steeply dipping rupture plane with up to 2 m of slip distributed over a single slip patch with dimensions of 20×20 km. The ~12 s long rupture expanded northward. Aftershocks occur at shallower depths than the mainshock slip zone.

Plain Language Summary The earthquake that struck on 30 November 2018, causing damage in Anchorage, Alaska, involved a fault rupture within the Pacific plate, which is sinking into the mantle beneath Alaska along the convergence zone between the Pacific and North American plates. Anchorage was seriously damaged during the great 1964 Alaska earthquake, which had a magnitude of 9.2 and resulted from sudden sliding on the shallow plate boundary; far less damage was produced by the 2018 event, which had a magnitude of 7.1 and involved deeper deformation of the underthrust slab. There is a lateral change in the dip of the sinking plate with the thick, relatively buoyant oceanic plateau called the Yakutat terrane having shallow dip to the east of the earthquake while normal thickness oceanic crust dips more steeply to the west. The 2018 event was located in the central region of the slab distortion. Intraslab events of this type present significant earthquake hazard, but it is difficult to determine their likelihood of occurrence.

1. Introduction

Earthquake hazards associated with plate convergence in subduction zones are largely related to faulting on the main plate boundary faults, or megathrusts. The deformation budgets for these events, controlled by relative plate motions and frictional strain accumulation, provide a basis for quantifying their hazards. However, earthquakes within the plates also present significant hazard and these events lack reliable deformation rate contexts for evaluating their hazard. Of particular note are large earthquakes that rupture within underthrust slabs of oceanic lithosphere at depths from 45 to 120 km or so, as these often locate below populated coastal regions. While not tsunamigenic like intraplate ruptures near the subduction trench and outer rise, the shaking hazard is high for this class of earthquakes, as the *P* and *S* waves go almost straight up into the populated zones (e.g., Ye et al., 2014).

The 30 November 2018 Anchorage, Alaska, earthquake is an example of such an event, as the epicenter locates about 12 km north of Anchorage (Figure 1), but the earthquake ruptured at depths of 45 to 65 km, placing it within the underthrust Pacific slab. The large magnitude of the earthquake, M_W 7.1, resulted in strong shaking across Anchorage and some extensive failures of engineered materials, including major roads, in low lying regions of saturated sediments. The shaking in Anchorage was the largest since the great 1964 Alaska earthquake (M_W 9.2), which was a massive plate boundary rupture. While it appears that relatively little structural damage occurred in the 2018 event (other than due to sediment slumping) in comparison to other near-urban earthquakes like the 1989 Loma Prieta, 1994 Northridge, and 1995 Kobe events, likely as a result of improved building codes adopted after the 1964 earthquake, this type of event is very difficult to plan for, as deformation rates within subducting slabs are much harder to

©2019. American Geophysical Union. All Rights Reserved.

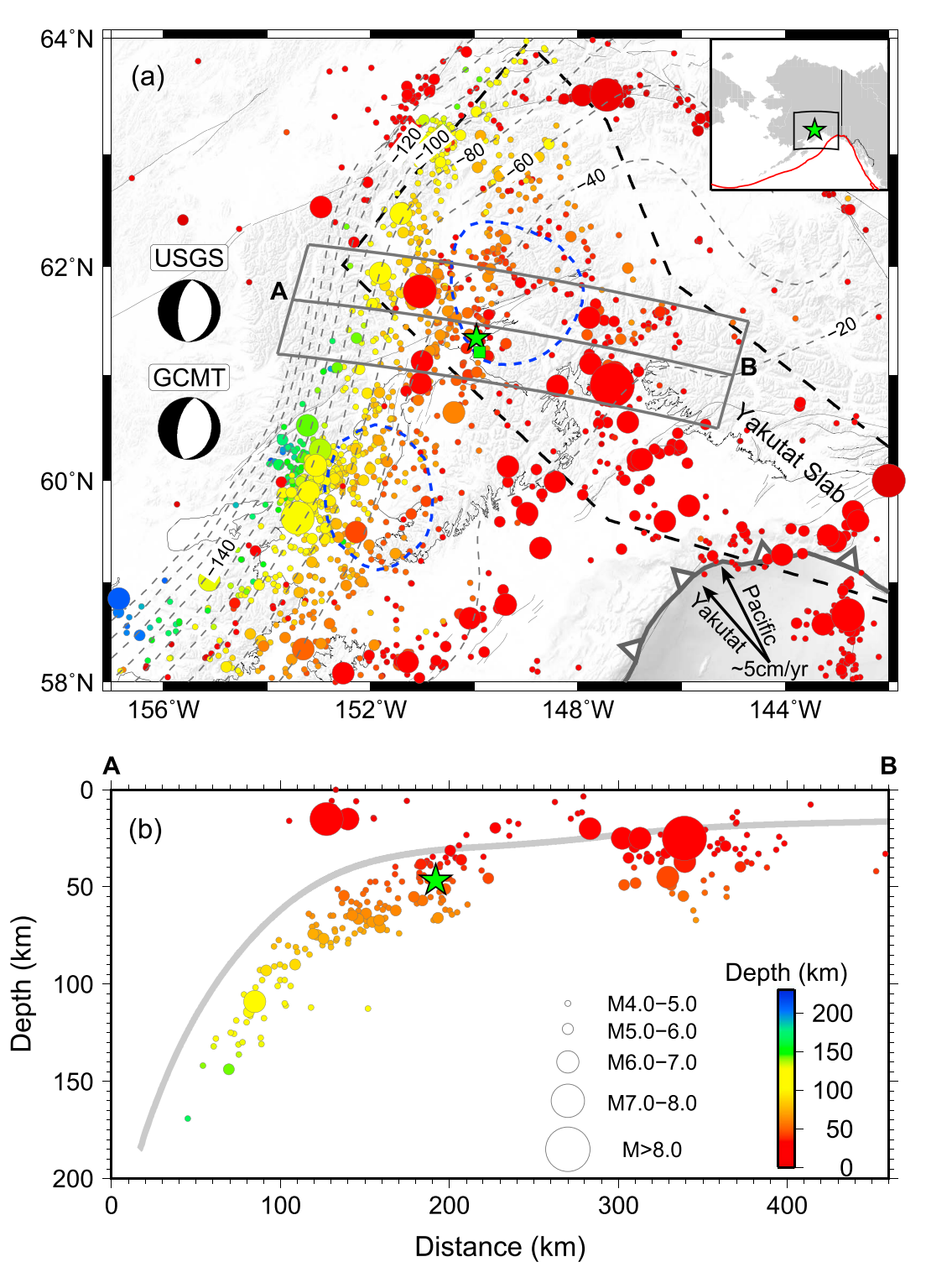


Figure 1. (a) The 30 November 2018 Anchorage earthquake source region, background seismicity, and regional plate tectonic setting (inset map indicates the North America-Pacific plate boundary in red). The green star is the epicenter of the Anchorage earthquake, and the focal mechanisms are the best-double couples of the USGS and gCMT solutions. The green square locates the city of Anchorage. Dots indicate the USGS National Earthquake Information Center historical earthquakes size and depth. Gray lines are active faults. Gray dashed lines indicate the plate interface depth contours for model Slab2 (Hayes et al., 2018). Blue dashed outlines locate two slow slip event regions (Fu et al., 2015; Wei et al., 2012). The black arrows show the plate motion relative to North America for the Pacific plate and Yakutat terrane (Li et al., 2018). The bold black dashed line highlights the Yakutat terrane, which underthrusts North America (Eberhart-Phillips et al., 2006; Kim et al., 2014). (b) Vertical profile cross-section oriented perpendicular to the strike of the fault geometry. The bold gray line indicates the plate interface for Slab2. gCMT = global Centroid-Moment Tensor.



constrain or monitor than deformation on plate boundaries. Other major intraplate earthquakes of this type have occurred in Chile (e.g., Delouis & Legrand, 2007), Taiwan (e.g., Kanamori et al., 2012), Sumatra (e.g., Wiseman et al., 2012), the Philippines (e.g., Ye et al., 2012), the western Aleutians (e.g., Ye et al., 2014), Mexico (e.g., Melgar et al., 2018; Ye et al., 2017), and in 1949, 1965, and 2001 under Washington State (e.g., Bustin et al., 2004). When located below populated areas, such events can be very damaging. The much smaller 3 October 1954 M \sim 6.4 Kenai intraplate earthquake at 61.5 km depth in the Pacific slab (ISC-GEM) produced MMI VIII shaking intensity on the western Kenai Peninsula (Brockman et al., 1988; Silwal et al., 2018).

The rupture process of the 2018 Anchorage earthquake is constrained here by inversion of seismic and geodetic observations to provide understanding of the nature of this damaging event. While difficult to quantify, the seismic hazard of this class of intraslab earthquakes for populated regions located above subducting slabs needs to be considered.

2. Data Processing, Fault Parameterization, and Inversion Strategy

The USGS National Earthquake Information Center (NEIC) reports the Alaskan Earthquake Center (AK) determination of the 30 November 2018 Anchorage earthquake hypocenter at 61.346°N, 149.955°W, 46.7 km deep at 17:29:29 UTC (USGS-NEIC, https://earthquake.usgs.gov/earthquakes/eventpage/ak20419010/executive). The event is located in a region of active crustal and slab deformation (supporting information Figure S1).

We select 46 *P* and 21 *SH* broadband teleseismic waveforms from the Incorporated Research Institutions for Seismology data archive based on good azimuthal coverage (Figure S2) and signal-to-noise ratio (Figures S3 and S4). Deconvolved ground displacements are then precisely aligned on *P* or *SH* wave first arrivals (Text S1 and Figures S3 and S4) and band-pass filtered from periods of 1 to 300 s before conducting inversions. Green's functions for teleseismic body wave are computed by incorporation of the reflection and refraction coefficient method and ray theory (Helmberger, 1974).

Numerous near-field seismic stations captured the coseismic process of the Anchorage earthquake. We select strong-motion records at 20 stations (Figure S5) from the USGS National Strong-Motion Project and Alaska Regional Network (AK), at epicentral distances less than 200 km. Given the uncertainty in local velocity structure, we use broadband displacement signals retrieved from the local records, which are less sensitive to inaccurate regional velocity structure. The strong-motion seismograms are doubly integrated using the procedure of Wang et al. (2011). Green's functions for the local seismic waveforms are generated using a frequency-wave number integration algorithm (Zhu & Rivera, 2002).

In addition, we select coseismic GPS static displacements at 44 sites (Figure S5) from 5-min position time series from continuously operating stations made available by the University of Nevada Reno (https://geodesy.unr.edu/). Due to the relatively large errors in the vertical components, only horizontal components are incorporated in finite-fault inversions. The Green's functions for the coseismic GPS displacements are generated using a generalized reflection-transmission coefficient matrix method (Xie & Yao, 1989).

The *W*-phase solution from the USGS-NEIC indicates almost pure double-couple normal faulting. One nodal plane dips east with strike = 6° , dip = 28° , and rake = -93° . The second nodal plane dips west with a strike = 189° , dip = 62° , and rake = -88° . The seismic moment estimate is $M_0 = 4.7 \times 10^{19}$ Nm (M_W 7.05). The rapid global Centroid-Moment Tensor solution (https://www.globalcmt.org/CMTsearch.html) has slightly larger $M_0 = 4.92 \times 10^{19}$ Nm (M_W 7.1) and a centroid depth of 53.8 km, with best-double-couple geometries of strike = $7^{\circ}/190^{\circ}$, dip = $30^{\circ}/60^{\circ}$, and rake = $-93^{\circ}/-88^{\circ}$. The centroid time shift is 6.5 s.

To determine the actual rupture plane, we initially construct fault models based on the two nodal planes of the USGS-NEIC *W*-phase solution. The first fault model (F1) has an east-dipping fault plane, and the second fault model (F2) has a west-dipping fault plane. The two fault planes have the same dimensions, 57 km along-strike and 45 km along-dip, divided into 285 square subfaults (3.0 by 3.0 km). We perform a series of finite-fault inversions using seismological and geodetic observations separately and jointly.

We apply a kinematic finite-fault inversion method (Ji et al., 2002) that carries out the waveform inversion in the wavelet domain, with a simulated annealing method to simultaneously resolve rake angle, rise time,



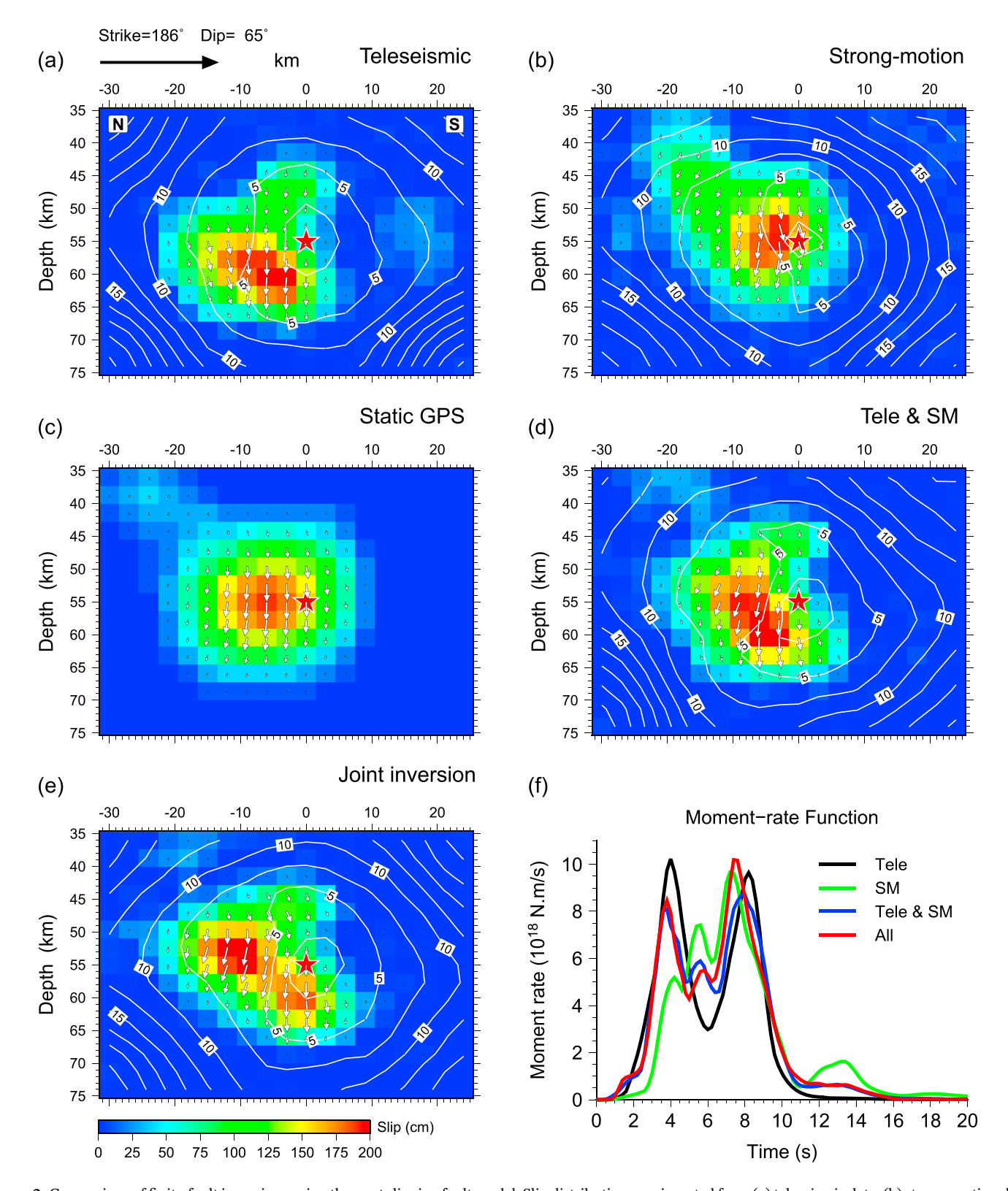


Figure 2. Comparison of finite-fault inversions using the west-dipping fault model. Slip distributions are inverted from (a) teleseismic data, (b) strong-motion data, (c) GPS static displacements, (d) teleseismic and strong-motions, and (e) all data sets jointly. The red star indicates the hypocenter, the color bar shows the scale of the slip amplitude, the white arrows represent the slip directions and the white contours outline the rupture propagation time in seconds. (f) Comparison of moment rate functions for each kinematic model.

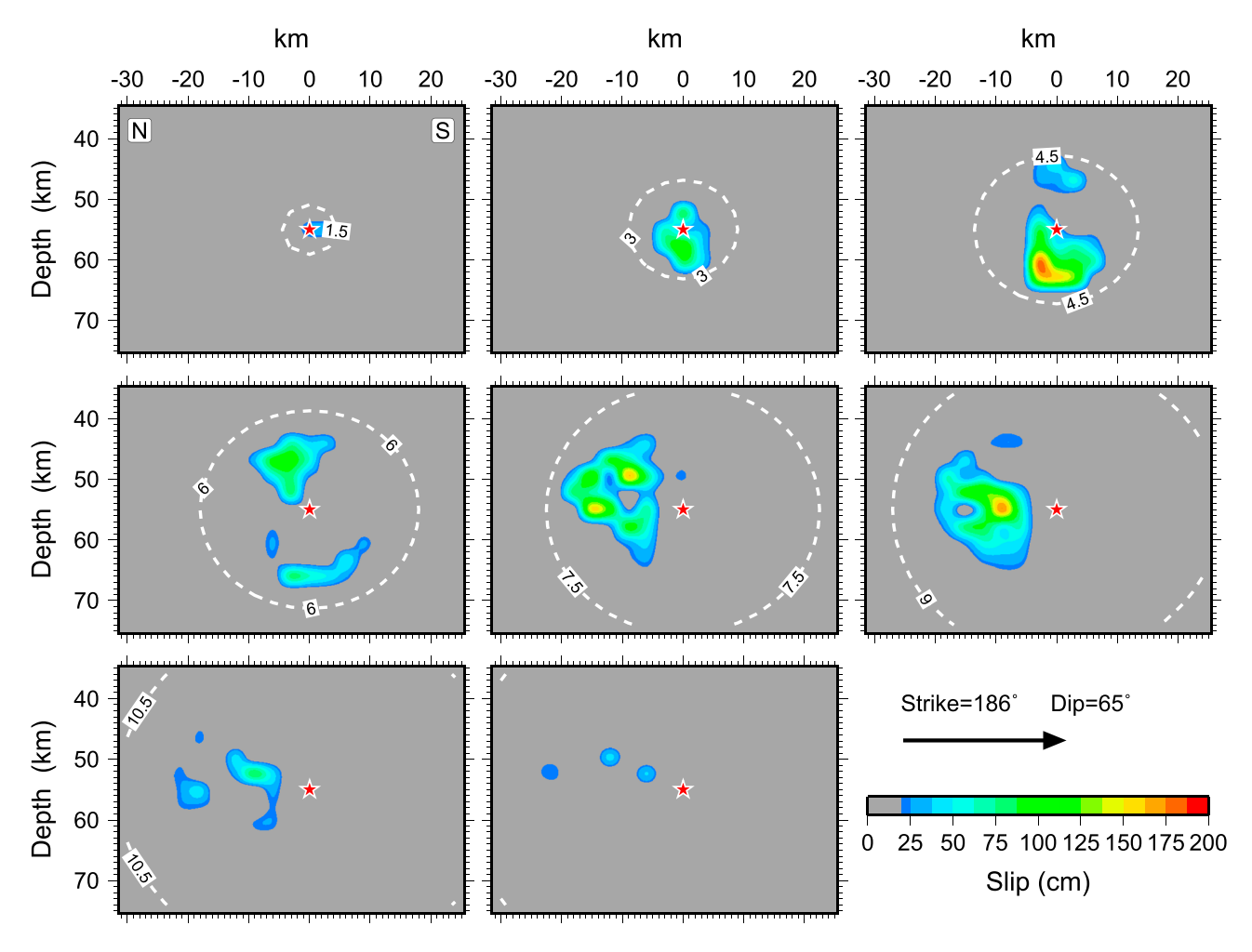


Figure 3. Snapshots of the west-dipping joint inversion with a time interval of 1.5 s. Color indicates the fault slip. The red star indicates the hypocenter and the white dashed contours denote the rupture front for a rupture velocity of 3.0 km/s.

slip amplitude, and average rupture velocity. During the inversions, the slip is allowed to vary from 0.0 to 4.0 m and the rise time of each subfault is constrained between 0.6 and 6.0 s. The rake angle is limited to between -60° and -120° . The rupture velocity varies from 0.75 to 3.75 km/s. We weight the seismological and geodetic data sets equally during the joint inversion, and also apply a smoothing constraint on the fault slip to stabilize the inversions (Ji et al., 2002). Green's functions for both the seismic and static observations are computed using a 1-D layered velocity model derived from van Stiphout et al. (2009; Figure S6).

3. Parameters Tests and Inversion Results

Accurate hypocenter location is an essential aspect of finite-fault inversion. To optimize this placement, we conduct a series of preliminary finite-fault inversions using teleseismic body waves to search for the optimal hypocenter depth. The inversion waveform misfit has a minimum value for a hypocenter at a depth of 55 km, somewhat deeper than the NEIC hypocenter of 46.7 km (Figure S7), which is associated with good alignment of *P* and *SH* depth phases calculated using our source velocity model. Moreover, to systematically explore the precise fault positioning, we perform joint inversions for different assumed hypocentral positions over a 0.05° spaced grid of longitude and latitude positions around the USGS-AK epicenter (Figure S8). Based on these tests, our models initiate rupture at a depth of 55 km beneath the USGS-NEIC epicenter (61.346°N, 149.955°W).



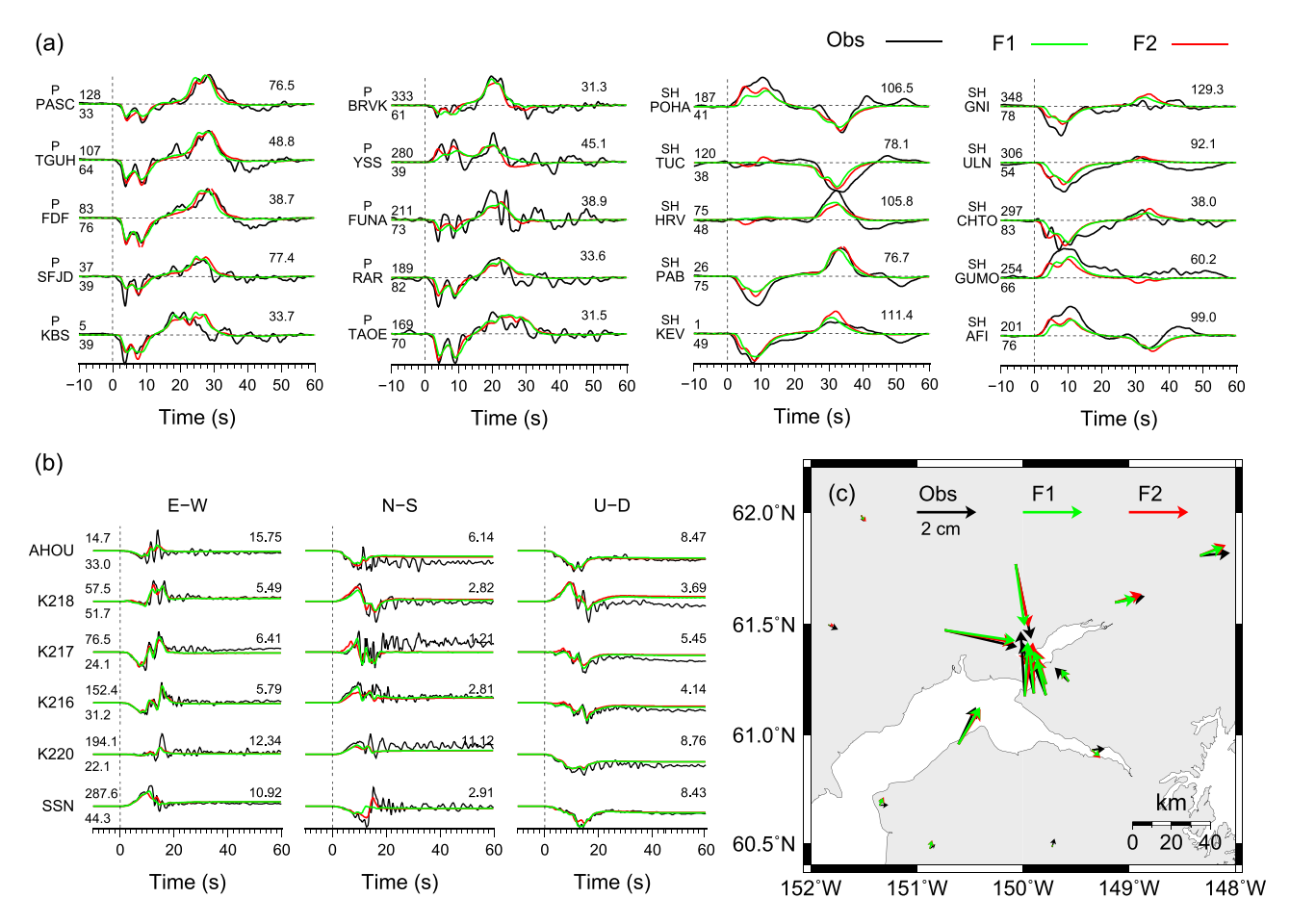


Figure 4. Comparison of subsets of the observed data and synthetics for the east-dipping model (green) and the west-dipping model (red). Panels (a) and (b) show teleseismic displacement and strong-motion displacement comparisons, respectively. The azimuth and epicentral distance for each station are indicated above and below the waveform leader, respectively. The number at the end of each record is the peak value of the observed data in micrometer for teleseismic and in centimeters for strong-motion data, respectively. (c) Comparison of coseismic static horizontal GPS displacements. Comparisons of all additional data and predictions are shown in Figures S16 to S18.

Attenuation affects the amplitude of seismic waves at teleseismic distances. For the Anchorage earthquake, we find that synthetic SH amplitudes are too low if we use a common average attenuation t_{β}^* value of 4.0 s. We perform inversions varying t_{β}^* from 1.0 to 4.0 s (Figure S9). Based on these inversions we set $t_{\beta}^* = 2.4$ s.

3.1. Nodal Plane 1: The East-Dipping Fault Plane

Using the east-dipping fault plane of the W-phase solution with dip of 28°, we invert for slip distributions using seismological and geodetic observations separately and jointly (Figures S10 to S12). These slip models all feature one slip patch, centered northeast of the hypocenter. The teleseismic model has a somewhat deeper rupture than other inversions, with a peak slip of ~2.0 m (Figure S10a). The joint model has a compact slip zone with a depth range of 50–60 km. Peak slip is centered about 10 km north of the hypocenter with an amplitude of ~2.3 m (Figure S10e). The rupture has an average velocity of ~3.0 km/s. The centroid location of the joint model is located 10 km NNE of the hypocenter (Figure S13) and has a depth of 54.7 km. The seismic moment $M_0 = 5.02 \times 10^{19}$ Nm (M_W 7.06) is slightly larger than the W-phase moment tensor solution. Detailed source parameters are listed in Table S1.

The inverted moment rate functions of the kinematic slip models are similar, as shown in Figure S10f. All indicate that \sim 90% of the moment is released within the first 10 s, concentrated in two stages of rupture. The early and late stages of rupture have relatively shorter rise time (\sim 2 s) compared with the middle stage (\sim 6 s; Figure S11), resulting in two peaks in the moment rate functions (Figure S10f). The rupture

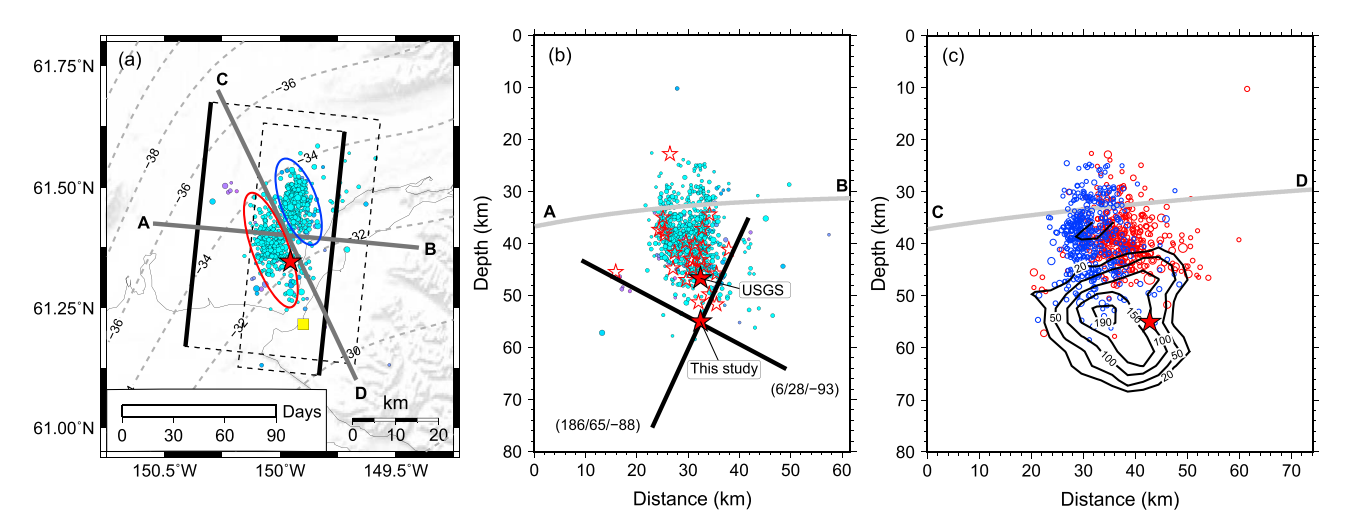


Figure 5. (a) The reviewed aftershock distribution within 3 months after the mainshock by USGS-AK. The two solid gray lines indicate locations of cross-sections. One is perpendicular to the strike of the fault models (AB), and the other separates the two groups of aftershocks outlined by red and blue ellipses (CD). The rectangles represent the surface projection of the two fault models. The gray dashed lines indicate contours of the plate interface depth from Slab2 (Hayes et al., 2018). The red star indicates the epicenter of the mainshock, and the yellow rectangle is the city of Anchorage. (b) Vertical cross-section of the aftershocks distribution along AB. Color denotes the differential origin time after the mainshock while size scales with magnitude. The solid black lines indicate the fault geometry of the two fault models. Aftershocks with magnitude larger than 4.0 are indicated with white-filled red stars. The solid stars highlight the hypocenter of the USGS-NEIC and this study. (c) Vertical cross-section of the aftershocks distribution along CD. The blue and red dots correspond to the two groups of aftershocks outlined in (a). The black contours indicate the slip distribution of the west-dipping model. The gray line indicates the plate interface.

essentially propagates unilaterally northward after initiation, breaking two major slip patches at 4.5 and 7.5 s (Figure S12), corresponding to the two shorter rise time stages. Using the average slip from finite-fault models, we estimate the static stress drop ($\Delta\sigma$) to be about 2.7 MPa based on the relations given in Kanamori and Anderson (1975; Text S2). Following the approach of Ye et al. (2016), we also calculate the energy-related stress drop ($\Delta\sigma_E$) weighted by slip larger than 0.2 m, finding $\Delta\sigma_E$ is 3.9 MPa (Text S2).

3.2. Nodal Plane 2: The West-Dipping Fault Plane

A similar suite of inversions is performed for the west-dipping fault plane. First we conduct a series of preliminary finite-fault inversions to evaluate the fault geometry. A fault plane with strike 186° and dip 65° slightly improves the data fitting relative to the point-source geometries. Inversions for this geometry show consistent slip distributions obtained for each data set, with one compact asperity, located adjacent to the hypocenter (Figure 2). The joint inversion has the main slip zone from 45 to 65 km depth, slightly larger in depth extent but narrower in horizontal extent than for the F1 models due to the larger dip. Rupture initiated with minor slip at 55 km depth and peak slip of 2.0 m. The centroid of the slip distribution is located about 10 km north of the hypocenter (Figure S13) at a depth of 54.4 km. The seismic moment is $M_0 = 5.01 \times 10^{19}$ Nm (M_W 7.06). Similar to the F1 models, ~90% of the moment released within the first 10 s (Figure 2f), with overall duration of ~12 s. Figure 3 shows snapshots of the joint west-dipping rupture model, indicating a complex rupture process. Relatively small slip locates near the hypocenter. During the first 6 s, the rupture propagated in the downdip direction, and then expanded unilaterally northward along strike. These two stages involve faster rupture velocity (~3.0 km/s) than the average (Figure 3) and shorter rise time (Figure S14). The static stress drop ($\Delta \sigma$) is 2.76 MPa and the energy-related stress drop ($\Delta \sigma_E$) weighted by slip larger than 0.2 m is 3.2 MPa. Figure S15 shows the stress change distributions for both joint models. Detailed source parameters for model F2 are listed in Table S1.

For both possible fault planes, the slip distribution is relatively compact and located northward from the hypocenter, indicating rupture away from Anchorage. A subset of the waveforms and static displacement fits is shown in Figure 4. Additional comparisons are shown in Figures S16 to S18. Both models match the main characteristics of the geodetic and seismological observations, and the difference of fitting errors is very small between the two models for separate and joint inversions (Table S2). The moment rate functions are very similar in both cases (Figures 2f and S10f). These two characteristics do not



distinguish which is the causative fault. Although we only forward model the coseismic surface vertical displacements, both models fit the vertical displacements well (Figure S19). The relatively large source depth and along-strike rupture propagation are the main reasons the fault plane is not readily identified. However, by careful examination of the actual waveform fits, the west-dipping fault plane is found to better explain details of the teleseismic data, especially the robust two-pulse character of the P waves (Figure S16), and slightly improves predicted depth phases (PP and SP phase). Overall, we prefer the west-dipping fault plane as the causative fault plane.

4. Discussion and Conclusions

The 2018 Anchorage earthquake involved intraslab rupture from 45 to 65 km deep with an east-west trending tension axis. The event is located in a region of strong lateral change in slab dip (Figure 1) resulting from underthrusting of the thick Yakutat terrane adjacent to normal oceanic plate. There are large differences in the inferred plate interface depth among different models, but Slab2 represents the lateral change as a smooth distortion. It is likely that the 2018 earthquake involved tearing of the plate caused by differences in buoyancy within the slab. Our preferred west-dipping solution for the faulting is consistent with the western portion of the slab, which dips more steeply, having moved downward relative to the buoyant eastern side. The complex distribution of faulting in the region (Figure S1) requires detailed modeling to confidently evaluate whether there is a tear or detachment along the intraslab margin of the Yakutat terrane.

Aftershock distributions often provide independent constraints on the faulting geometry, slip heterogeneity, and stress perturbation caused by the main shock. Figure 5a shows the surface projection of the USGS-AK reviewed aftershock sequence of the 2018 Anchorage earthquake. The spatial distribution of aftershocks has a northeast-southwest pattern, which can be separated into two groups; one group located north of the hypocenter, with greater depth extent (blue circles in Figure 5c), and another group northwest of the hypocenter with a somewhat broader spatial distribution (red circles in Figure 5c). The overall distribution corresponds to the rupture dimensions for both models F1 and F2 (Figure S13). The vertical extension of reviewed aftershocks is limited within a range from 25 to 55 km (Figure 5b). If the depths hold up with future more precise relocation efforts, the aftershock sequence may rupture through the slab (assuming Slab2 in accurate). Vertical profile AB indicates that larger aftershocks (white-filled red stars) have a hint of a west-dipping trend (Figure 5b) consistent with our preferred fault geometry. However, the aftershocks are mostly shallower than the slip zone, which precludes using the patterns to constrain the slip distribution, as apparent in Figure 5c. Aftershock patterns for intraplate ruptures are often complex and indicate activation of activity on faults other than the main rupture plane (e.g., Melgar et al., 2018; Ye et al., 2012, 2014). The aftershock distribution coincides with the strong curvature of the upper slab interface in Slab2, along the intraplate transition from Pacific to Yakutat slab (Figure 5a; Kim et al., 2014). Lu et al. (1997) conducted detailed analyses of stress directions in the Alaska subduction zone using fault plane solutions and defined a normal faulting regime in the source region of the 2018 Anchorage earthquake at depths of 40-60 km. It is reasonable to infer that intraslab distortion is responsible for occurrence of the event. Future work may reveal clearer structure in the aftershock distribution that may help to define the main rupture plane.

Major intraslab faulting events like the 2018 Anchorage earthquake present a difficult challenge to earthquake hazard analysis, as their infrequency suggests low deformation rates and results in a lack of historical activity with which to make statistical assessments. However, the observed widespread occurrence of such events warrants their consideration for seismic and landslide hazard assessments in coastal regions along subduction zones. Evaluation of global occurrence rates may be the best approach to this difficult problem, as there is an accumulating inventory of documented major intraslab ruptures of this type.

Acknowledgments

Teleseismic body wave recordings were downloaded from the Incorporated Research Institutions for Seismology (IRIS) data management center (https://ds.iris.edu/wilber3/find_ event). Strong-motion recording were obtained from the USGS National Strong-Motion Project (NSMP) (https:// earthquake.usgs.gov/monitoring/ nsmp/) and Alaska Regional Network (AK) (https://www.fdsn.org/networks/ detail/AK/). GPS displacements were obtained from the Nevada Geodetic Laboratory (NGL, https://geodesy.unr. edu/), which obtained the raw GPS data from continuously operating GPS stations operated by the Plate Boundary Observatory. We thank Editor Gavin Hayes, and reviewers Jeff Freymueller and Carl Tape for helpful comments on the manuscript. C. Liu was supported by National Key R & D Program on Monitoring, Early Warning and Prevention of Major Natural Disaster (2017YFC1500305) and the Visiting Scholar Program of the Chinese Science Council. T. Lay's research on earthquakes is supported by U.S. National Science Foundation grant EAR1802364. All figures were generated using the open-source Generic Mapping Tools software (Wessel & Smith, 1991).

References

Brockman, S. R., Espinosa, A. F, & Michael, J. A. (1988). Catalog of intensities and magnitudes for earthquake in Alaska and the Aleutian Islands—1786-1981. U. S. Geological Survey Bulletin 1840.

Bustin, A., Hyndman, R. D., Lambert, A., Ristau, J., He, J., Dragert, H., & Van der Kooij, M. (2004). Fault parameters of the Nisqually earthquake determined from moment tensor solutions and the surface deformation from GPS and InSAR. *Bulletin of the Seismological Society of America*, 94, 363–376. https://doi.org/10.1785/0120030073

Delouis, B., & Legrand, D. (2007). M_W 7.8 Tarapaca intermediate depth earthquake of 13 June 2005 (northern Chile): Fault plane identification and slip distribution by waveform inversion. *Geophysical Research Letters*, 34, L01304. https://doi.org/10.1029/2006GL028193



- Eberhart-Phillips, D., Christensen, D. H., Brocher, T. M., Hansen, R., Ruppert, N. A., Haeussler, P. J., & Abers, G. A. (2006). Imaging the transition from Aleutian to Yakutat collision in central Alaska, with local earthquakes and active source data. *Journal of Geophysical Research*, 111, B11303. https://doi.org/10.1029/2005JB004240
- Fu, Y., Liu, Z., & Freymueller, J. T. (2015). Spatiotemporal variations of the slow slip event between 2008 and 2013 in the southcentral Alaska subduction zone. *Geochemistry, Geophysics, Geosystems*, 16, 2450–2461. https://doi.org/10.1002/2015GC005904
- Hayes, G. P., Moore, G. L., Portner, D. E., Hearne, M., Flamme, H., Furtney, M., & Smoczyk, G. M. (2018). Slab2, a comprehensive subduction zone geometry model. Science, 362(6410), 58–61. https://doi.org/10.1126/science.aat4723
- Helmberger, D. V. (1974). Generalized ray theory for shear dislocations. Bulletin of the Seismological Society of America, 64(1), 45-64.
- Ji, C., Wald, D. J., & Helmberger, D. V. (2002). Source description of the 1999 Hector Mine, California, earthquake, Part I: Wavelet domain inversion theory and resolution analysis. Bulletin of the Seismological Society of America, 92(4), 1192–1207. https://doi.org/10.1785/ 0120000916
- Kanamori, H., & Anderson, D. L. (1975). Theoretical basis of some empirical relations in seismology. Bulletin of the Seismological Society of America, 65(5), 1073–1095.
- Kanamori, H., Lee, W. H. K., & Ma, K.-F. (2012). The 1909 Taipei earthquake—Implications for seismic hazard in Taipei. *Geophysical Journal International*, 191, 126–146. https://doi.org/10.1111/j.1365-246X.2012.05589.x
- Kennett, B. L. N., & Engdahl, E. R. (1991). Traveltimes for global earthquake location and phase identification. *Geophysical Journal International*, 105(2), 429–465. https://doi.org/10.1111/j.1365-246X.1991.tb06724.x
- Kim, Y.-H., Abers, G. A., Li, J., Christensen, D., Calkins, J., & Rondenay, S. (2014). Alaska Megarthrus 2: Imaging the megathrust zone and Yakutat/Pacific plate interface in the Alaska subduction zone. *Journal of Geophysical Research: Solid Earth*, 119, 1924–1941. https://doi.org/10.1002/2013JB010581
- Li, H., Wei, M., Li, D., Liu, Y., Kim, Y., & Zhou, S. (2018). Segmentation of slow slip events in south central Alaska possibly controlled by a subducted oceanic plateau. *Journal of Geophysical Research: Solid Earth*, 123, 418–436. https://doi.org/10.1002/2017JB014911
- Lu, Z., Wyss, M., & Pulpan, H. (1997). Details of stress directions in the Alaska subduction zone from fault plane solutions. *Journal of Geophysical Research*, 102(B3), 5385–5402. https://doi.org/10.1029/96JB03666
- Melgar, D., Ruiz-Angulo, A., Garcia, E. S., Manea, M., Manea, V. C., Xu, X., et al. (2018). Deep embrittlement and complete rupture of the lithosphere during the MW 8.2 Tehuantepec earthquake. *Nature Geoscience*, 11, 955–960. https://doi.org/10.1038/s41561-018-0229-y
- Silwal, V., Tape, C., & Lomax, A. (2018). Crustal earthquakes in the Cook Inlet and Susitna region of southern Alaska. *Tectonophysics*, 745, 245–263. https://doi.org/10.1016/j.tecto.2018.08.013
- van Stiphout, T., Kissling, E., Wiemer, S., & Ruppert, N. (2009). Magmatic processes in the Alaska subduction zone by combined 3-D b value imaging and targeted seismic tomography. *Journal of Geophysical Research*, 114, B11302. https://doi.org/10.1029/2008JB005958
- Wang, R., Schurr, B., Milkereit, C., Shao, Z., & Jin, M. (2011). An improved automatic scheme for empirical baseline correction of digital strong-motion records. *Bulletin of the Seismological Society of America*, 101(5), 2029–2044. https://doi.org/10.1785/0120110039
- Wei, M., McGuire, J. J., & Richardson, E. (2012). A slow slip event in the south central Alaska subduction zone and related seismicity anomaly. *Geophysical Research Letters*, 39, L15309. https://doi.org/10.1029/2012GL052351
- Wessel, P., & Smith, W. H. (1991). Free software helps map and display data. Eos, Transactions American Geophysical Union, 72(41), 441–446. https://doi.org/10.1029/90EO00319
- Wiseman, K., Banerjee, P., Bürgmann, R., Sieh, K., Dreger, D. S., & Hermawan, I. (2012). Source model of the 2009 M_W 7.6 Padang intraslab earthquake and its effect on the Sunda megathrust. *Geophysical Journal International*, 190, 1710–1722. https://doi.org/10.1111/j.1365-246X.2012.05600.x
- Xie, X., & Yao, Z. (1989). A generalized reflection-transmission coefficient matrix method to calculate static displacement field of a dislocation source in a stratified half space. *Chinese Journal of Geophysics*. 32. 191–205.
- Ye, L., Lay, T., Bai, Y., Cheung, K. F., & Kanamori, H. (2017). The 2017 MW 8.2 Chiapas, Mexico, earthquake: Energetic slab detachment. Geophysical Research Letters, 44, 11,824–11,832. https://doi.org/10.1002/2017GL076085
- Ye, L., Lay, T., & Kanamori, H. (2014). The 23 June 2014 M_W 7.9 Rat Islands archipelago, Alaska, intermediate depth earthquake. Geophysical Research Letters, 41, 6389–6395. https://doi.org/10.1002/2014GL061153
- Ye, L., Lay, T., & Kanamori, H. (2012). Intraplate and interpolate faulting interactions during the August 31, 2012, Philippine Trench earthquake (M_W 7.6) sequence. Geophysical Research Letters, 39, L24310. https://doi.org/10.1029/2012GL054164
- Ye, L., Lay, T., Kanamori, H., & Rivera, L. (2016). Rupture characteristics of major and great (M_W ≥ 7.0) megathrust earthquakes from 1990 to 2015: 1. Source parameter scaling relationships. *Journal of Geophysical Research: Solid Earth*, 121, 826–844. https://doi.org/10.1002/2015JB012426
- Zhu, L., & Rivera, L. A. (2002). A note on the dynamic and static displacements from a point source in multilayered media. *Geophysical Journal International*, 148(3), 619–627. https://doi.org/10.1046/j.1365-246X.2002.01610.x